International Journal on
Technical and Physical Problems of Engineering
(IJTPE)
Published by International Organization of IOTPE

ISSN 2077-3528
IJTPE Journal
www.iotpe.com
ijtpe@iotpe.com

September 2026 | Issue 68 | Volume 18 | Number 3 | Pages 126-135

NUMERICAL ASSESSMENT OF NANOFLUID-ENHANCED COLD-PLATE COOLING FOR HIGH-RATE LITHIUM-ION BATTERY OPERATION

S. Rahmoune [1] L. Belarche [1] S. Elhamdani [2] Z. Lafdaili [3] S. Panchal [4]

1. Laboratory of Mechanics, Processes, Energy and Environment, Ibn Zohr University, Agadir, Morocco
said.rahmoune@edu.uiz.ac.ma, l.belarche@uiz.ac.ma
2. Laboratory of Fluid Mechanics and Energy Engineering, Faculty of Sciences Semlalia, Cadi Ayyad University, Marrakech, Morocco, selhamdani@gmail.com
3. Engineering for Smart and Sustainable Systems Research Centre, Mohamed V University, Rabat, Morocco
lafdaili@emi.ac.ma
4. Chemical Engineering Department, University of Waterloo, Waterloo, Ontario, Canada
satyam.panchal@uwaterloo.ca

Abstract- Thermal management remains a critical challenge for lithium-ion batteries operating under high discharge conditions. This study investigates the influence of key operating parameters, including the nanofluid inlet temperature, nanoparticle type and concentration, on the thermal behavior of a dual cold-plate cooling system applied to a 20 Ah lithium-ion cell under 4C discharge conditions. The optimal configuration is achieved using a 3% CuO-WEG nanofluid at an inlet temperature of 25 °C. Under these conditions, the maximum cell temperature is reduced to 38.5 °C, corresponding to a decrease of approximately 4 °C compared to the base fluid, while the maximum temperature gradient ($\Delta T_{\max}$) remains below 2 °C, ensuring a uniform thermal distribution across the cell. In addition, the average Nusselt number increases by up to 22% relative to the case without nanoparticles. These findings demonstrate the strong potential of nanofluid-based cooling for advanced battery thermal management, improving both thermal regulation and temperature uniformity during 4C discharge of lithium-ion batteries.

Keywords: Nanofluid, Lithium-Ion Battery, Cold Plate, Thermal Management System.

1. INTRODUCTION

The rapid expansion of electric vehicle (EV) technologies has intensified interest in lithium-ion batteries (LiBs) owing to their high energy density and power capability [z1]. In parallel, previous investigations showed that integrating battery storage with demand-response strategies can improve energy efficiency and reduce operational costs [2], while LiBs also contribute to mitigating greenhouse gas emissions in transportation systems [3]. Despite these advantages, battery performance remains strongly dependent on thermal conditions, making heat management a critical issue in EV applications.

During high charge/discharge operations, excessive heat generation may drive the cell beyond its recommended operating range, accelerating aging and degrading electrochemical performance. In addition, non-uniform temperature fields inside the battery promote localized material deterioration and reduce service life [4]. Capasso et al. [5] reported that LiBs operate most effectively between 20 °C and 40 °C, where thermal stability and cycle durability are preserved. Outside this range, thermal stresses combined with severe operating conditions considerably increase the risk of degradation and thermal runaway [6]. Consequently, the development of efficient battery thermal management systems (BTMS) has become essential for ensuring both safety and long-term reliability.

Several BTMS technologies have been investigated, including air cooling, liquid cooling, phase change materials, and heat pipe systems [7]. Among them, liquid cooling has demonstrated superior heat dissipation capability and better temperature uniformity compared with conventional air-based methods [8]. Recent studies have therefore focused on improving liquid-cooling performance through optimized cold-plate geometries and advanced working fluids. Mahesh et al. [9] experimentally and numerically examined a dual cold-plate configuration and highlighted the strong influence of coolant inlet temperature, flow rate, and channel geometry on thermal regulation and pressure losses.

To further enhance convective heat transfer, nanofluids have attracted increasing attention in battery cooling applications. Ref. [10] reported that nanoparticle-enhanced coolants can substantially reduce battery surface temperature relative to conventional base fluids. Other investigations also demonstrated noticeable improvements in heat transfer performance and thermal uniformity when nanofluids are employed [11]. Nevertheless, increasing nanoparticle concentration generally raises fluid viscosity, resulting in higher hydraulic resistance and pumping power requirements [12]. This introduces a thermo-

Registered: 260421 Article Info: 260323 Accepted: 240811
Reserved: 240714 Available: 260930

hydraulic compromise that must be carefully evaluated when designing high-performance cooling systems.

Although previous studies have examined nanofluid cooling and cold-plate configurations separately, the coupled effects of nanoparticle type, particle concentration, and coolant inlet temperature under high discharge rates remain insufficiently explored, particularly for dual cold-plate systems operating at 4C conditions.

Accordingly, the present work numerically investigates the thermal behavior of a dual cold-plate cooling system applied to a 20 Ah lithium-ion pouch cell. Water-ethylene glycol (WEG) nanofluids containing CuO and Al_2O_3 nanoparticles are considered. The influence of nanoparticle type, concentration, and inlet temperature is analyzed in terms of maximum battery temperature, temperature uniformity, and heat transfer enhancement.

2. PROBLEM DEFINITION AND MATHEMATICAL MODEL

Figures 1a and 1b illustrate the side and front schematic views, respectively, of the liquid cooling system employing double cold plates for a 20 Ah lithium-ion pouch cell. The battery is positioned between two cold plates incorporating internal flow channels which the coolant circulates. The flow arrangement consists of alternating inlet and outlet channels to promote effective heat removal.

The geometric dimensions of battery are 227 mm in length, 160 mm in width, and 7.25 mm in thickness. The considered lithium-ion cell under has a capacity of 20 Ah and a nominal voltage of 3.3 V. Figure 1c illustrates the detailed geometry of the cold plate, where the maximum channel width is 3 mm. The hydraulic diameter for the channel is defined as D_h=1.54 mm.

$$D_h = \frac{4A_{ch}}{P_{ch}} \tag{1}$$

where, A_{ch} represents the cross-sectional flow area of the channel and P_{ch} denotes the wetted perimeter.

To optimize computation, the battery's thermal and physical characteristics, cold plates, and coolant are assumed to be homogeneous, isotropic, and to exhibit constant thermophysical properties. The corresponding material properties are summarized in Table 1. For the nanofluid, all properties are considered constant except for density, which is modeled using, the Boussinesq approximation. The thermophysical properties of base fluid are listed in Table 2.

Table 1. Properties of lithium-ion battery, and cold plate [9]

Parameter	Lithium-ion	Cold plate
Density (kg/m^3)	1940	2702
Specific heat capacity (J/kg.K)	1000	903
Thermal conductivity (W/m.K)	18.2	237
Specific energy (Wh kg)	131	-
Energy density (Wh/L)	247	-
Nominal energy (Wh)	65	-
Nominal capacity (Ah)	20	-
Electrolyte	Carbonate based	-
Anode material	Graphite	-
Cathode material	$LiFePO_4$	-
Electrolyte	Carbonate based	-

Table 2. Properties of WEG base fluid and nanoparticles

Nano-particle / Based fluid	ρ (kg/m^3)	k (W/m.K)	μ (mPa.s)	C_p (J/kg.K)	Ref.
WEG	1059.68	0.404	2.96	3468	[13]
CuO	6500	18	-	540	[14]
Al_2O_3	3890	30.0	-	880	[13]

3. CFD MODEL

3.1. Conservation Equations

The thermal behavior of the system is modeled as a conjugate heat transfer problem involving both solid and fluid domains. Heat transfer within the battery is governed by conduction with internal heat generation, whereas the cold plate is modeled as solid regions with pure conduction and no volumetric heat source. The coolant flow is described by the conservation equations of mass and momentum, coupled with the energy equation to account for convective heat transfer. Turbulence effects are modeled using the standard k-epsilon (k-ε) turbulence models. As reported by [15], the k-ε model is widely adopted due to its numerical stability and its ability to capture the global heat transfer behavior, although its accuracy may be limited in near-wall regions.

The heat generation rate (Q_{gen}) of lithium-ion battery is determined using the COMSOL-based model, following the formulation provided in the COMSOL theory documentation. The adopted lumped approach considers only the ohmic overpotential, neglecting activation and concentration overpotentials, and does not explicitly account for electrochemical reactions within the battery. Equation (2) defines the Reynolds number, which is used to characterize the flow regime within cooling channels. It is expressed as:

$$Re = \frac{\rho_{nf} v_{nf} D_h}{\mu_{nf}} \tag{2}$$

where, ρ_{nf} is the nanofluid density, v_{nf} is the mean flow velocity, D_h is the hydraulic diameter, and μ_{nf} is the dynamic viscosity. For all simulated cases, the Reynolds number satisfies $Re \geq 2818$, indicating a turbulent flow regime.

The turbulence effects are modeled using k-ε within the Reynolds-Averaged Navier-Stokes (RANS) approach, with a prescribed turbulence intensity of 5%. The governing equations are formulated in the Cartesian coordinate system (x, y, z) and are presented in Equations (3)-(11) [14].

$$\frac{\partial(\rho_b c_{p,b} T_b)}{\partial t} = k_b\left(\frac{\partial^2 T_b}{\partial x^2} + \frac{\partial^2 T_b}{\partial y^2} + \frac{\partial^2 T_b}{\partial z^2}\right) + Q_{gen} \tag{3}$$

$$\frac{\partial(\rho_c c_{p,c} T_c)}{\partial t} = k_c\left(\frac{\partial^2 T_c}{\partial x^2} + \frac{\partial^2 T_c}{\partial y^2} + \frac{\partial^2 T_c}{\partial z^2}\right) \tag{4}$$

$$\frac{\partial(\rho_{nf})}{\partial t} + \frac{\partial(\rho_{nf} v_{nf})}{\partial x} + \frac{\partial(\rho_{nf} v_{nf})}{\partial y} + \frac{\partial(\rho_{nf} v_{nf})}{\partial z} = 0 \tag{5}$$

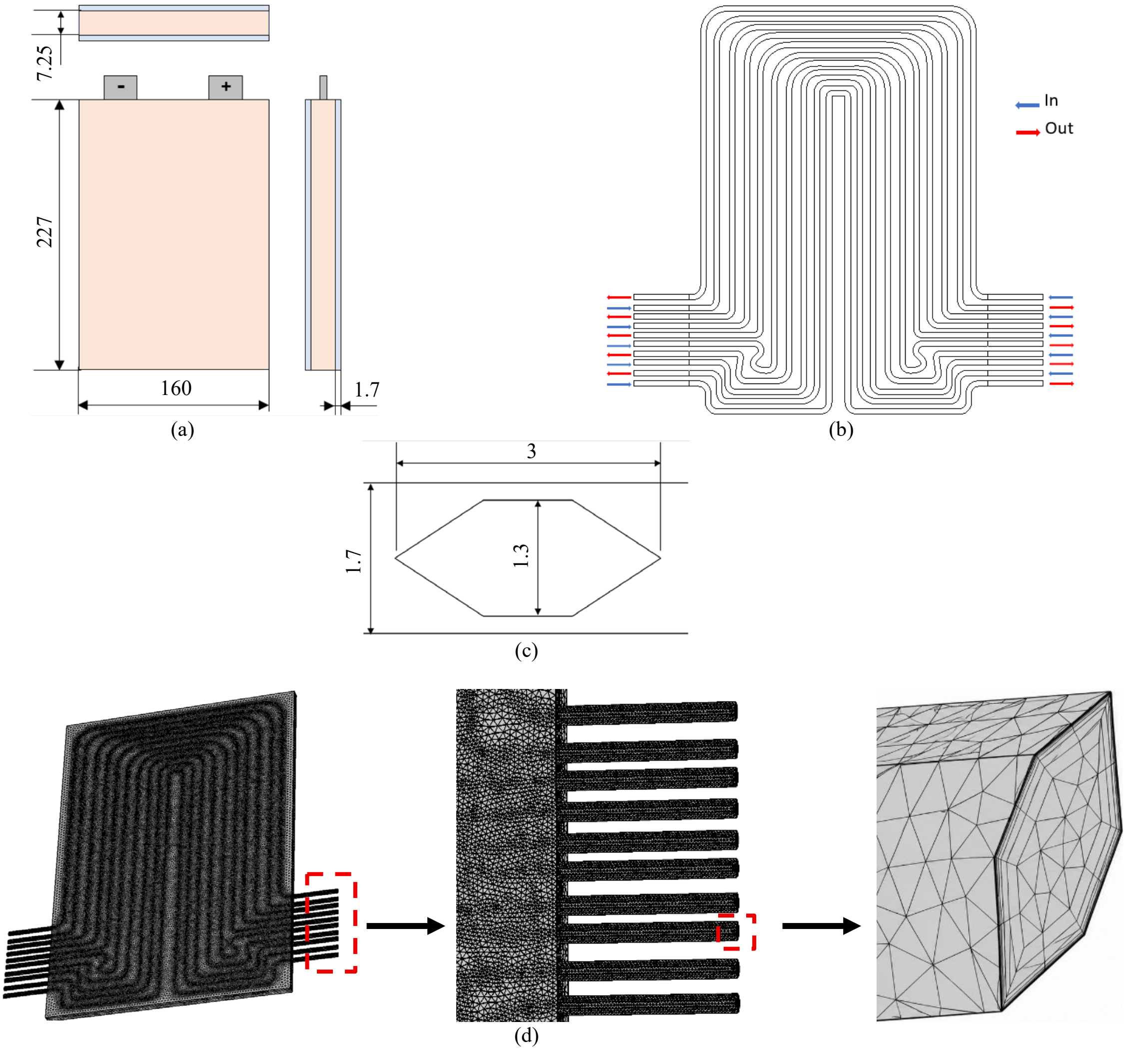

Figure 1. (a) Numerical model of a 20 Ah lithium-ion pouch cell with dual cold plates, (b) cold plate geometry schematic with 10 cooling channels and coolant flow direction, (c) channel geometry with a maximum width of 3 mm, (d) and mesh configuration

$$\rho_{nf} C_{p,nf} \frac{\partial(T_{nf})}{\partial t} + \frac{\partial(\rho_{nf} C_{p,nf} v_{nf} T_{nf})}{\partial x} + \frac{\partial(\rho_{nf} C_{p,nf} v_{nf} T_{nf})}{\partial y} + \frac{\partial(\rho_{nf} C_{p,nf} v_{nf} T_{nf})}{\partial z} = k_{n,f}\left(\frac{\partial^2 T_{nf}}{\partial x^2} + \frac{\partial^2 T_{nf}}{\partial y^2} + \frac{\partial^2 T_{nf}}{\partial z^2}\right) \tag{6}$$

$$\frac{\partial(\rho_{nf})}{\partial t} u_{nf} + \frac{\partial(\rho_{nf} u_{nf})}{\partial x} + \frac{\partial(\rho_{nf} u_{nf})}{\partial y} + \frac{\partial(\rho_{nf} u_{nf})}{\partial z} = \frac{\partial p}{\partial x}\left(\frac{\partial^2 u_{nf}}{\partial x^2} + \frac{\partial^2 u_{nf}}{\partial y^2} + \frac{\partial^2 u_{nf}}{\partial z^2}\right) \tag{7}$$

$$\frac{\partial(\rho_{nf})}{\partial t} v_{nf} + \frac{\partial(\rho_{nf} v_{nf})}{\partial x} + \frac{\partial(\rho_{nf} v_{nf})}{\partial y} + \frac{\partial(\rho_{nf} v_{nf})}{\partial z} = \frac{\partial p}{\partial x}\left(\frac{\partial^2 v_{nf}}{\partial x^2} + \frac{\partial^2 v_{nf}}{\partial y^2} + \frac{\partial^2 v_{nf}}{\partial z^2}\right) \tag{8}$$

$$\frac{\partial(\rho_{nf})}{\partial t} w_{nf} + \frac{\partial(\rho_{nf} w_{nf})}{\partial x} + \frac{\partial(\rho_{nf} w_{nf})}{\partial y} + \frac{\partial(\rho_{nf} w_{nf})}{\partial z} = \frac{\partial p}{\partial x}\left(\frac{\partial^2 w_{nf}}{\partial x^2} + \frac{\partial^2 w_{nf}}{\partial y^2} + \frac{\partial^2 w_{nf}}{\partial z^2}\right) \tag{9}$$

$$\begin{aligned} &\frac{\partial(\rho_k)}{\partial t} + \frac{\partial(\rho_{nf} V_{nf} k)}{\partial x} + \frac{\partial(\rho_{nf} V_{nf} k)}{\partial y} + \frac{\partial(\rho_{nf} V_{nf} k)}{\partial z} = \frac{\partial}{\partial x}\left(\left(\mu_{nf} + \frac{\mu_t}{\sigma_k}\right)\frac{\partial k}{\partial x}\right) + \frac{\partial}{\partial y}\left(\left(\mu_{nf} + \frac{\mu_t}{\sigma_k}\right)\frac{\partial k}{\partial y}\right) + \\ &+ \frac{\partial}{\partial z}\left(\left(\mu_{nf} + \frac{\mu_t}{\sigma_k}\right)\frac{\partial k}{\partial z}\right) + G_k + G_{buo} - \rho_{nf}\varepsilon - Y_M - S_M \end{aligned} \tag{10}$$

$$\begin{aligned} &\frac{\partial(\rho_\varepsilon)}{\partial t} + \frac{\partial(\rho_{nf} V_{nf} \varepsilon)}{\partial x} + \frac{\partial(\rho_{nf} V_{nf} \varepsilon)}{\partial y} + \frac{\partial(\rho_{nf} V_{nf} \varepsilon)}{\partial z} = \frac{\partial}{\partial x}\left(\left(\mu_{nf} + \frac{\mu_t}{\sigma_k}\right)\frac{\partial \varepsilon}{\partial x}\right) + \frac{\partial}{\partial y}\left(\left(\mu_{nf} + \frac{\mu_t}{\sigma_k}\right)\frac{\partial \varepsilon}{\partial y}\right) + \\ &+ \frac{\partial}{\partial z}\left(\left(\mu_{nf} + \frac{\mu_t}{\sigma_k}\right)\frac{\partial \varepsilon}{\partial z}\right) + C_1 \frac{\varepsilon}{k_{nf}}(G_k + C_3 G_b) - C_2 \rho_{nf} \frac{\varepsilon^2}{k} + S_\varepsilon \end{aligned} \tag{11}$$

The turbulent (or eddy) viscosity is determined using the following equation [18]:

$$\mu_t = C_\mu \rho_{nf} \frac{k_{nf}^2}{\varepsilon} \tag{12}$$

The following expression is used to determine the dynamic viscosity [14]:

$$\mu_{nf} = C_\mu \frac{\mu_{nf}}{(1-\phi_p)^{2.5}} \tag{13}$$

According to the Maxwell-Garnett model, the effective thermal conductivity of the nanofluid, is given by [14]:

$$k_{nf} = k_f [\frac{(k_p + 2k_f) - 2\phi_p (k_f - k_p)}{(k_p + 2k_f) + \phi_p (k_f - k_p)}] \tag{14}$$

The Boussinesq approximation is employed to model density fluctuations arising from temperature gradients. The nanofluid density, and heat capacity are expressed by the succeeding relation [14].

$$\rho_{nf} = (1-\phi_p)\rho_f + \phi_p \rho_p \tag{15}$$

$$Cp_{nf} = (1-\phi_p)Cp_f + \phi_p Cp_p \tag{16}$$

The average pressure drop (ΔP_{avg}) over all channels are calculated using the following equations, where ΔP_n represents the pressure drop in a single channel [18].

$$\Delta P_{avg} = \frac{\sum_{n=1}^{10} \Delta P_n}{10} \tag{17}$$

$$\Delta P_n = P_{out,n} - P_{in,n} \tag{18}$$

3.2. Validation of the Code

The numerical model was validated against the experimental and computational results reported by Patil et al. [9] to verify its capability in predicting the thermal behavior of the dual cold-plate cooling configuration. The computational domain consists of three coupled regions: the lithium-ion battery, the cooling plates, and the coolant channels. Heat conduction was solved within the solid regions, whereas fluid flow and convective heat transfer inside the channels were governed by the continuity, momentum, and energy equations. The simulations were performed using COMSOL Multiphysics under the operating conditions corresponding to Test No. 4 [9].

Water was employed as the coolant with an inlet temperature of 5 °C and a volumetric flow rate of 350 ml/min. The numerical assessment relied on several thermal and hydraulic indicators, including the average pressure drop (ΔP_{avg}), average heat transfer coefficient (HTC_{avg}), average Nusselt number (Nu_{avg}), and the maximum and minimum battery temperatures. Relative deviation was adopted to quantify the agreement between the present predictions and the reference data. In addition, the predicted isothermal contours were compared with those reported in the validation study to examine the consistency of the thermal field distribution. The corresponding comparisons are summarized in Table 3 and Figure 2.

The obtained deviations remain below 2.5% for all evaluated parameters, confirming the good agreement between the present model and the reference results. The predicted temperature contours also reproduce the same thermal distribution pattern observed in the reference article values [9], particularly regarding the progressive temperature evolution along the cooling channels and the localization of high-temperature regions. Such consistency demonstrates that the developed model accurately captures the coupled heat transfer and flow mechanisms governing the investigated battery cooling system.

The validation results therefore confirm the reliability of the numerical approach for predicting both thermal and hydraulic characteristics of the dual cold-plate configuration under the investigated operating conditions.

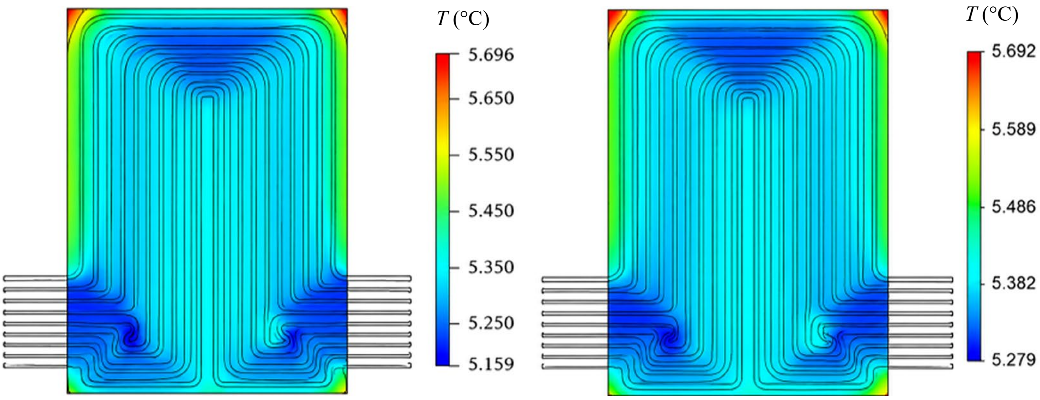

Figure 2. (a) Simulated isotherm contours, and (b) isotherm contours from the validation study [9]

3.3. Initial and Boundary Conditions

In this study, the inlet volumetric flow rate of the nanofluid was fixed at 800 ml/min, while the nanoparticle volume fraction ranged from 1% to 4%. The inlet temperature was maintained at T_{in}=25 °C. At the outlet, a zero relative static pressure condition was imposed, using atmospheric pressure as the reference pressure.

A no-slip boundary condition was applied to all solid walls assumed to be adiabatic, thereby neglecting heat exchange with the environment. These boundary conditions were selected to represent realistic operating conditions while ensuring numerical stability and accuracy of the simulations.

Table 3. Comparative of simulated and reference results

Indicator	Reference Article Values [9]	Simulation Values	Relative Error (%)
ΔP_{avg} (KPa)	38.856	37.352	−3.87
HTC_{avg}	19.0440	19.3617	−1.67
Nu_{avg}	48.3200	49.1300	−1.68
$T_{\max}$ (°C)	5.6920	5.6960	0.08
$T_{\min}$ (°C)	5.2790	5.1590	−2.28

Table 4. Mesh type

Mesh Type	Number of Nodes	Number of Elements
TEST 1	1 049 045	3 063 774
TEST 2	1 420 070	4 130 578
TEST 3	1 821 243	5 723 652
TEST 4	2 190 725	6 437 981
TEST 5	4 136 801	11 620 921
TEST 6	5 064 119	14 706 034

3.4. Grid Independency Test

The cold plate domain was discretized using a mesh with a base element size of 2 mm and a minimum element size of 0.9 mm. For the nanofluid channels, a target mesh size of 0.55 mm and a minimum size of 0.2 mm were adopted. To accurately resolve the thermal and hydrodynamic boundary layers, an inflation layer with a thickness of 0.5 µm was introduced along the fluid-solid interfaces. In addition, nine inflation layers with a growth rate of 1.85 were employed in the near-wall regions.

A grid independence study was performed using six different mesh configurations to evaluate the numerical stability and mesh sensitivity of the model. Table 4 summarizes the corresponding numbers of nodes and elements for each mesh configuration. For mesh type 4, the variation in the average temperature was only 0.0071% when the number of nodes increased from 2,190,725 to 4,136,801, as illustrated in Figure 4. This negligible variation confirms that the numerical solution becomes independent of the mesh beyond this refinement level. Consequently, mesh type 4 was chosen for all subsequent simulations.

4. RESULT AND DISCUSSION

This section analyzes the thermal performance of the dual cold-plate cooling system using the average heat transfer coefficient (HTC_{avg}) and the average Nusselt number (Nu_{avg}). The heat transfer rate is given by [16].

$$Q_{conv,n} = m_{in,n} Cp_{nf} (T_{out,n} - T_{in,n}) \tag{19}$$

The heat transfer coefficient (HTC) is determined from Equation (20) [16]. In this formulation, the numerator represents the convective heat transferred from the wall to the fluid, whereas the denominator accounts for the convective surface area and the logarithmic mean temperature difference between the wall and the bulk fluid.

$$HTC_n = \frac{Q_{conv,n}}{A_{wall,n}(T_{wall,n} - T_{in,n})_{LMTD,n}} \tag{20}$$

$$(T_{wall,n} - T_{in,n})_{LMTD,n} = \frac{(T_{out,n} - T_{in,n})}{\log[\frac{(T_{wall,n} - T_{in,n})}{(T_{wall,n} - T_{out,n})}]} \tag{21}$$

For a single cooling channel, the Nusselt number is expressed as:

$$Nu_n = \frac{HTC_n D_{h,n}}{k_{nf}} \tag{22}$$

Considering all channels within the cold plate, the average Nusselt number is evaluated as follows [16]:

$$Nu_{avg} = \frac{\sum_{n=1}^{10} Nu_n}{10} \tag{23}$$

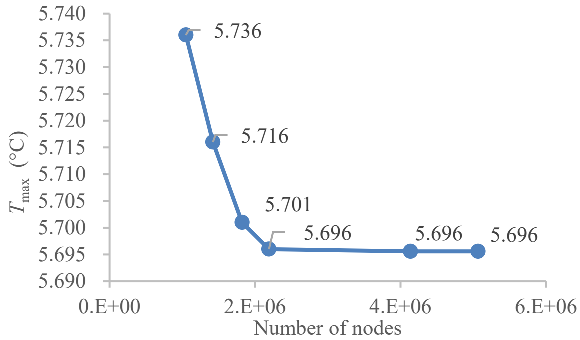

Figure 3. Grid independency test

The analysis focuses on the influence of inlet coolant temperature (25 °C, 30 °C, and 35 °C) and nanoparticle volume fraction (0-4%) using CuO-WEG and Al_2O_3-WEG nanofluids. The inlet volumetric flow rate is maintained constant at 800 ml/min throughout all simulations. A total of 27 numerical simulations were conducted to evaluate the cooling performance under different operating conditions. The thermal behavior of the battery is assessed using performance indicators, including the maximum temperature ($T_{\max}$), minimum temperature ($T_{\min}$), maximum temperature difference ($\Delta T_{\max} = T_{\max} - T_{\min}$), and the average Nusselt number (Nu_{avg}). These parameters provide insight into both heat dissipation capability and temperature uniformity within battery cell.

4.1. Impact of Inlet Coolant Temperature

To evaluate the influence of coolant inlet temperature independently from flow conditions, the volumetric flow rate of the CuO-WEG nanofluid was maintained constant at 800 ml/min throughout the analysis. Figure 4a illustrates the evolution of the average Nusselt number (Nu_{avg}) as a function of nanoparticle concentration. For all investigated inlet temperatures, Nu_{avg} increases with particle loading, confirming the enhancement of convective heat transfer produced by nanoparticle dispersion. The highest heat-transfer performance is obtained at 25 °C, where lower coolant temperature promotes stronger thermal exchange between the cold plate and the battery surface. A similar tendency is observed at 30 °C, although the corresponding Nu_{avg} values remain slightly lower. Beyond a concentration of 3%, the increase in Nu_{avg} becomes more pronounced, mainly due to the combined effect of improved effective thermal conductivity and intensified convective transport within the nanofluid. At 35 °C, the lowest heat-transfer levels are initially recorded; however, a significant rise in Nu_{avg} appears for concentrations exceeding 3%, indicating that higher particle loading partially compensates for the deterioration in cooling capacity caused by elevated inlet temperature.

The variation of the maximum battery temperature (T_{max}) is presented in Figure 4b. At inlet temperatures of 25 °C and 30 °C, only limited reductions in T_{max} are observed as nanoparticle concentration increases, suggesting moderate thermal enhancement under these operating conditions. In contrast, the highest temperatures occur at 35 °C, where T_{max} decreases from 40.393 °C for the base fluid to 40.049 °C at 4% concentration. The reduction becomes more evident above 2% nanoparticle loading, reflecting the stronger contribution of the nanofluid to heat removal at elevated thermal conditions. Nevertheless, the cooling performance at 35 °C remains less effective than that achieved at lower inlet temperatures.

Figure 4c shows the evolution of the maximum temperature difference (ΔT_{max}), which characterizes temperature uniformity inside the cell. At 25 °C and 30 °C, ΔT_{max} remains below 0.75 °C, indicating relatively homogeneous thermal distribution. At 35 °C, considerably larger thermal gradients are observed, with ΔT_{max} decreasing slightly from 4.324 °C to 4.151 °C as the nanoparticle concentration increases from 0% to 4%. Although the improvement remains moderate, the addition of nanoparticles contributes to reducing localized heat accumulation and improving thermal uniformity.

The isothermal contours displayed in Figure 5 further confirm the strong influence of inlet coolant temperature on battery thermal regulation. At 25 °C, the temperature field is relatively uniform, and the maximum temperature remains limited to 36.8 °C, reflecting efficient heat dissipation. Increasing the inlet temperature to 30 °C intensifies heat accumulation and raises the peak temperature to 39.2 °C, accompanied by steeper thermal gradients. At 35 °C, thermal concentration becomes more severe, with T_{max} reaching 41.5 °C, indicating a substantial decline in cooling effectiveness. The corresponding isotherms reveal weaker thermal regulation and reduced capability of the cooling system to maintain homogeneous temperature distribution at high inlet temperatures.

Overall, inlet coolant temperature significantly affects the thermal behavior of the battery cooling system. Increasing nanoparticle concentration enhances heat-transfer characteristics, particularly at concentrations above 3%. However, elevated inlet temperatures still deteriorate cooling effectiveness by increasing both T_{max} and ΔT_{max}. The results therefore demonstrate that efficient battery thermal management requires a coupled optimization of coolant temperature and nanoparticle concentration to achieve both effective heat dissipation and acceptable thermal uniformity under 4C discharge conditions.

4.2. Impact of the Inlet Nanofluid Type

The influence of nanoparticle material on the cooling performance was examined using CuO-WEG and Al_2O_3-WEG nanofluids under identical operating conditions, with a fixed inlet flow rate of 800 ml/min and an inlet temperature of 25 °C.

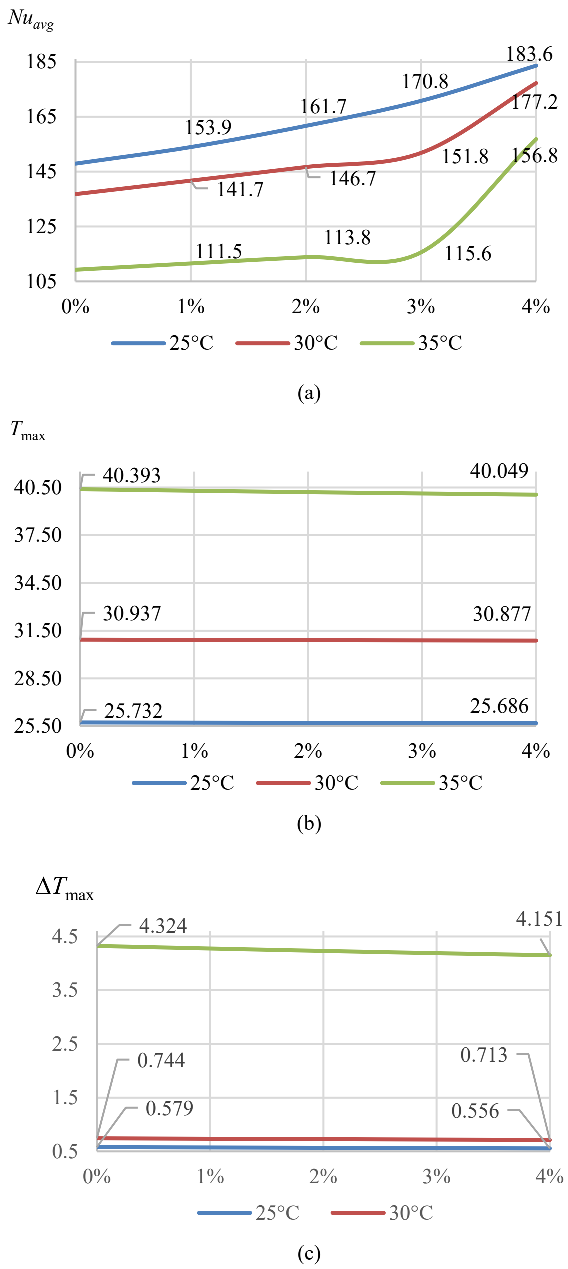

Figure 4. (a) Variation of the average Nusselt Number (Nu_{avg}), (b) Maximum battery temperature (T_{max}), and (c) maximum temperature difference (ΔT_{max}) under different inlet coolant temperatures

The thermal response of both nanofluids reveals a clear dependence on particle concentration. As illustrated in Figure 6a, the average Nusselt number increases continuously with increasing volume fraction for both suspensions, confirming the beneficial role of nanoparticles in enhancing convective heat transfer. Nevertheless, the enhancement remains more pronounced for CuO-WEG, particularly beyond 2% concentration.

At high particle loading ($\phi_p \geq 3\%$), CuO-WEG exhibits a sharper rise in Nu_{avg}, indicating stronger thermal transport capability compared with Al_2O_3-WEG. This behavior is mainly associated with the superior thermal conductivity of CuO nanoparticles, which intensifies heat diffusion within the coolant and improves energy exchange at the cold-plate interface.

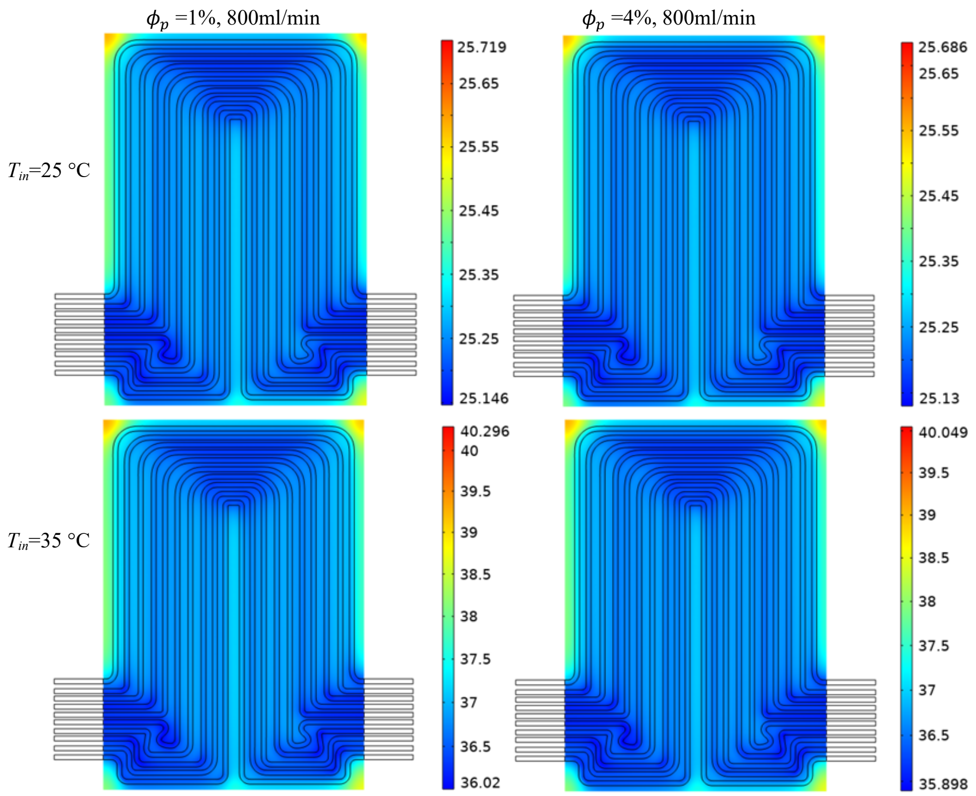

Figure 5. Temperature contours of the lithium-ion battery for different inlet coolant temperatures

The impact of nanoparticle type on battery peak temperature is presented in Figure 6b. For both nanofluids, increasing particle concentration progressively lowers $T_{\max}$, demonstrating the contribution of nanoparticle dispersion to heat removal enhancement. At low concentration (ϕ_p = 1%), the thermal difference between the two coolants remains relatively limited. However, as the concentration increases, CuO-WEG produces a more substantial temperature reduction, with the minimum $T_{\max}$ obtained at 4% concentration. The stronger cooling capability of CuO-WEG reflects its enhanced thermal transport characteristics, which promote more effective extraction of heat generated during battery operation.

A similar tendency is observed for the maximum temperature difference ($\Delta T_{\max}$) shown in Figure 6c. Increasing nanoparticle concentration improves temperature uniformity for both nanofluids by reducing internal thermal gradients. However, CuO-WEG achieves a more noticeable decrease in $\Delta T_{\max}$, especially for concentrations exceeding 2%, indicating better thermal homogenization inside the battery cell. In contrast, Al_2O_3-WEG provides only moderate improvement at high particle fractions. These results suggest that the thermal conductivity enhancement produced by CuO nanoparticles contributes not only to lowering the overall battery temperature, but also to mitigating localized heat accumulation.

The isothermal contours reported in Figure 7 further support these observations. At ϕ_p = 1%, CuO-WEG reduces the maximum battery temperature by approximately 2.8%, whereas Al_2O_3-WEG achieves a reduction of 1.9%. When the concentration reaches 3%, the temperature reduction increases to 4.2% for CuO-WEG compared with 3.1% for Al_2O_3-WEG. Moreover, CuO-WEG decreases the thermal gradient by nearly 0.5 °C, resulting in a more uniform temperature field throughout the pouch cell. The corresponding isotherms reveal lower heat concentration zones and improved thermal spreading when CuO nanoparticles are employed. In general, both nanofluids contribute to improving the thermal behavior of the dual cold-plate cooling system. Nevertheless, CuO-WEG consistently provides superior heat-transfer enhancement, lower peak temperature, and improved thermal uniformity relative to Al_2O_3-WEG, particularly at elevated nanoparticle concentrations. Under 4C discharge conditions, CuO-WEG demonstrates superior suitability for high-rate lithium-ion battery thermal management due to its enhanced heat dissipation capability and improved temperature uniformity.

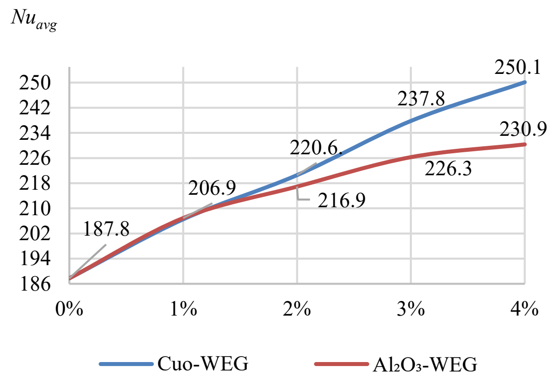

(a)

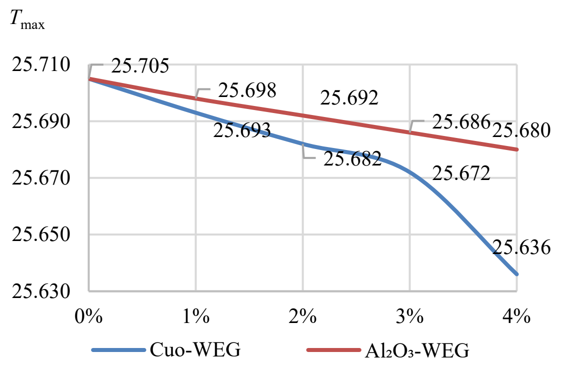

(b)

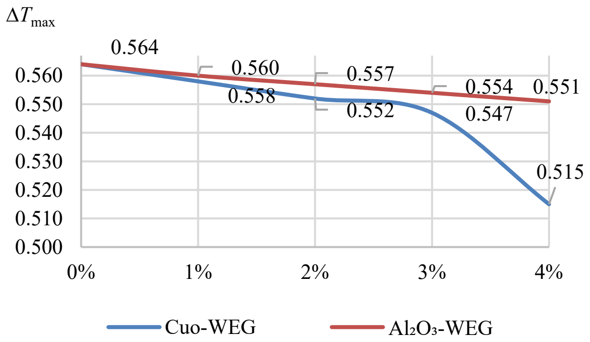

(c)

Figure 6. (a) Variation of the average Nusselt (Nu_{avg}), (b) Maximum temperature (T_{max}) of the battery, and (c) maximum temperature difference (ΔT_{max}) for different nanofluids

5. CONCLUSION

Efficient thermal regulation remains a critical requirement for lithium-ion batteries operating under high discharge conditions, where excessive heat generation and temperature non-uniformity accelerate performance degradation and reduce operational safety. The present investigation examined the combined influence of coolant inlet temperature, nanoparticle concentration, and nanofluid type on the thermal behavior of a dual cold-plate cooling system applied to a 20 Ah lithium-ion pouch cell under 4C discharge conditions.

The numerical results demonstrate that coolant inlet temperature strongly governs the overall cooling effectiveness. Among the investigated cases, an inlet temperature of 25 °C provides the most favorable thermal performance by maintaining lower battery temperatures and improved thermal uniformity. Increasing the inlet temperature progressively weakens the cooling capability due to the reduction in the thermal driving gradient between the battery surface and the coolant. As a result, the highest thermal accumulation is obtained at 35 °C, where T_{max} reaches 40.39 °C and ΔT_{max} exceeds 4 °C, indicating deterioration of thermal homogeneity inside the cell.

Nanoparticle addition enhances convective heat transfer for both investigated nanofluids, particularly at elevated particle concentrations. However, CuO-WEG consistently outperforms Al_2O_3-WEG owing to its superior thermal transport characteristics. Under the investigated conditions, the CuO-WEG nanofluid with a 3% concentration achieves the most effective thermal regulation, reducing Tmax by approximately 4.2% while simultaneously improving temperature uniformity within the battery.

Overall, the obtained findings demonstrate the effectiveness of CuO-based nanofluids in enhancing heat dissipation and temperature uniformity in lithium-ion batteries under 4C discharge conditions.

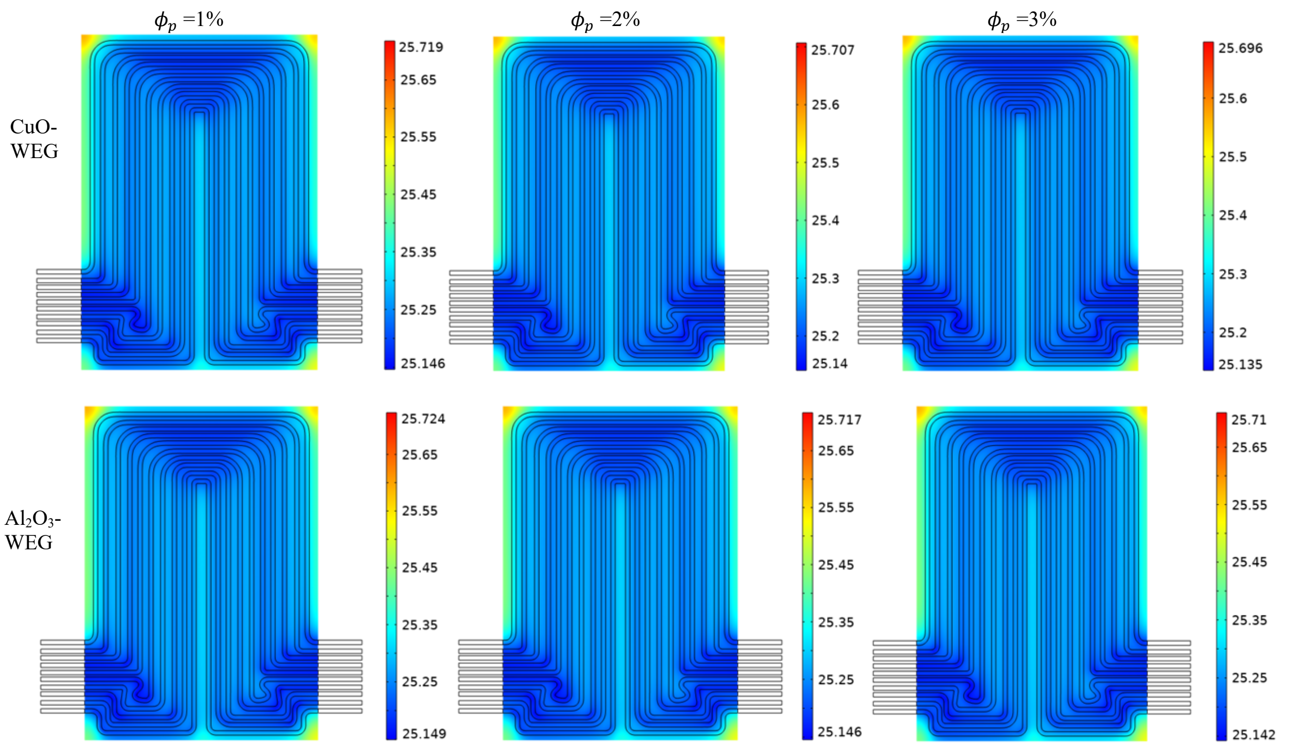

Figure 7. The temperature distribution of the lithium-ion battery for CuO-WEG and Al_2O_3-WEG

NOMENCLATURES

1. Acronyms

LIB Lithium-ion battery
BTMS Battery thermal management system
PCM Phase Change Material
EV Electric Vehicle
WEG Water-ethylene glycol
LMTD Logarithmic mean, temperature difference
HTC Heat transfer coefficient, [W.m^{-2}.K^{-1}]

2. Symbols / Parameters

c : Cold plate
b : Base fluid
nf : Nanofluid
p : Nanoparticle
D_h : Hydraulic diameter, [mm]
Q_{gen} : Heat generation rate, [W]
Nu_{avg} : Average Nusselt number
T : Temperature, [°C]
ΔT : Temperature difference, [°C]
P : Pressure, [Pa]
u, v, w : Nanofluid velocity, [m.s^{-1}]
C_1, C_2, C_3, C_μ : Model constant
C_p : Specific heat, [J.kg^{-1}.K^{-1}]
k : Thermal conductivity, [W.m^{-1}.K^{-1}]
ρ : Volumetric mass density, [kg.m^{-3}]
μ, ν : Kinematic and Dynamic fluid viscosity
σ_k, ε_k : Turbulent Prandtl numbers for k, and for ε
ϕ_p : Nanoparticle volume fraction

REFERENCES

[1] S. Bukhari, J. Maqsood, “Comparison of Characteristics of Lead-Acid, Nickel-Based, Lead-Crystal and Lithium-Based Batteries”, The 17th UKSim-AMSS International Conference on Modelling and Simulation, Paper No. 69, Cambridge, UK, 2015.
[2] H.A. Shayanfar, H. Shayeghi, L. Bagherzadeh, “Analyzing Demand Response Program in Residential Energy Hub Operation”, International Journal on Technical and Physical Problems of Engineering (IJTPE), Iss. 56, Vol. 15, No. 3, pp. 263-269, September 2023.
[3] M. Patil, S. Panchal, N. Kim, M. Lee, “Cooling Performance Characteristics of 20 Ah Lithium-Ion Pouch Cell with Cold Plates along Both Surfaces”, Energies, Vol. 11, No. 10, Article 2550, 2018.
[4] X. Gu, Y. Zhang, Z. Liu, H. Wang, J. Chen, “Structural Optimization and Battery Temperature Prediction of Liquid Cooling System for Lithium-Ion Battery Pack”, Case Studies in Thermal Engineering, Vol. 60, Article 104779, 2024.
[5] C. Capasso, T. Castiglione, D. Perrone, L. Sequino, “Thermal Management of Li-Ion Batteries: Experimentally Validated Model of Active Temperature Control Strategies with Liquid Cooling and Multi-Objective Optimization”, Journal of Energy Storage, Vol. 128, Article 117254, 2025.
[6] M. Soltani, J. Ronsmans, J. Jagumont, J. Van Mierlo, “A Three-Dimensional Thermal Model for a Commercial Lithium-Ion Capacitor Battery Pack with Non-Uniform Temperature Distribution”, Proceedings of the IEEE International Conference on Industrial Technology (ICIT), pp. 1126-1131, Melbourne, Australia, 2019.
[7] M. Qianjun, W. Yanglun, “Recent Development of Thermal Heat Storage Technology Coupling with Phase Change Material”, Journal of Energy Storage, Vol. 139, Article 118739, 2025.
[8] Y. Zhang, H. Liu, X. Chen, Z. Wang, J. Li, “A Novel Thermal Management System for Lithium-Ion Battery Modules Combining Direct Liquid Cooling with Forced Air Cooling”, Applied Thermal Engineering, Vol. 232, Article 120992, 2023.
[9] M.S. Patil, J.-H. Seo, S. Panchal, M. Lee, “Numerical Study on Sensitivity Analysis of Factors Influencing Liquid Cooling with Double Cold-Plate for Lithium-Ion Pouch Cell”, International Journal of Energy Research, Vol. 44, No. 14, p. 11244, 2020.
[10] Q. Liu, F. Liu, S. Liu, Y. Wang, S. Panchal, M. Fowler, R. Fraser, J. Yuan, J. Zhao, “Improved Performance of Li-Ion Battery Thermal Management System by Ternary Hybrid Nanofluid”, Journal of Energy Storage, Vol. 109, Article 115234, 2025.
[11] E. Yousefi, V. Talele, U. Morali, D. Mishra, D. Ramasamy, K. Kadirgama, “Liquid Immersion Cooling with Enhanced Al_2O_3 Nanofluid for Large-Format Prismatic Battery Pack: Numerical and Statistical Investigation”, Journal of Thermal Analysis and Calorimetry, Vol. 150, No. 1, pp. 1-19, 2025.
[12] N. Om, R. Zulkifli, P. Gunnasegaran, “The Influence of Different Types of Nanofluids on Thermal and Fluid Flow Performance of Liquid Cold Plate”, International Journal of Engineering and Technology, Vol. 7, No. 4.35, pp. 148-152, 2018.
[13] B. Rahmatinejad, “Investigating Thermophysical Properties and Thermal Performance of Al_2O_3 Nanoparticles in Water and Ethylene Glycol Based Fluids”, Journal of Nanostructures, Vol. 12, No. 3, pp. 642-659, 2022.
[14] Z. Lafdaili, S. El-Hamdani, A. Bendou, K. Limam, “Numerical Study of the Turbulent Natural Convection of Nanofluids in a Partially Heated Cubic Cavity”, Thermal Science, Vol. 25, No. 4A, pp. 2741-2752, 2021.
[15] E. Akbay, B. Dereli, O. Turgut, “The Effect of Turbulence Model and Nanofluid on Fluid Flow and Heat Transfer in a Narrow Rectangular Duct”, Politeknik Dergisi, Vol. 23, No. 2, pp. 567-579, 2020.
[16] M. Al Shdaifat, R. Zulkifli, K. Sopian, A. Salih, “Effect of CuO/Water Nanofluid as a Coolant for Liquid Cold Plate on Electric Vehicle Battery Cells”, Energy Sources, Part A: Recovery, Utilization, and Environmental Effects, Vol. 46, No. 1, p. 2270, 2024.

BIOGRAPHIES

Name: **Said**
Surname: **Rahmoune**
Birthday: 09.09.1988
Birthplace: Midelt, Morocco
Bachelor: Mechanical Engineering, National School of Electricity and Mechanics, Hassan II University, Casablanca, Morocco, 2010
Master: Mechanical Engineering, National School of Electricity and Mechanics, Hassan II University, Casablanca, Morocco, 2012
Ph.D.: Student, Mechanics and Energy Engineering, Laboratory of Mechanics, Processes, Energy and Environment, Ibn Zohr University, Agadir, Morocco, Since 2022
Scientific Position: Lecturer, OFPPT Training Complex, Agadir, Morocco, Since 2019
Research Interests: Thermal Management of Batteries
Scientific Publications: 1 Paper, 2 Books, 4 Projects

Name: **Lahoucine**
Surname: **Belarche**
Birthday: 27.03.1968
Birthplace: Tiznit, Morocco
Bachelor: Mechanical Engineering, Higher Normal School of Technical Education, Mohamed V University, Rabat, Morocco, 2008
Master: Energy, Process and Energy Engineering, National School of Applied Science, Ibn Zohr University, Agadir, Morocco, 2010
Ph.D.: Energy, Fluid Mechanics, Energetics, and Thermo-Dynamics, National School of Applied Science, Ibn Zohr University, Agadir, Morocco, 2015
Scientific Position: Prof., Mechanical Engineering, National School of Applied Science, Ibn Zohr University, Agadir, Morocco, Since 2017
Research Interests: Heat and Mass Transfer
Scientific Publications: 24 Papers, 5 Projects, 1 Thesis

Name: **Sakina**
Surname: **Elhamdani**
Birthday: 09.01.1978
Birthplace: Marrakech, Morocco
Bachelor: Hydraulics, Hydrology, Ibn Tofail University, Kenitra, Morocco, 1998
Master: Hydraulics, Hydrology, and Water Resources Pollution, Ibn Tofail University, Kenitra, Morocco, 2000
Ph.D.: Physics, Cadi Ayyad University, Marrakech, Morocco, 2006
Scientific Position: Prof., Fluid Mechanics and Environment, National School of Applied Sciences, Ibn Zohr University, Agadir, Morocco, Since 2008
Research Interests: Heat and Mass Transfer, Indoor Air Quality, Atmospheric Pollution
Scientific Publications: 24 Papers, 3 Projects, 1 Thesis

Name: **Zakaria**
Surname: **Lafdaili**
Birthday: 03.11.1983
Birthplace: Marrakech, Morocco
Bachelor: Mechanical Engineering, Mohammedia School of Engineers, Mohammed V University, Rabat, Morocco, 2004
Master: Mechanical Engineering, Mohammedia School of Engineers, Mohammed V University, Rabat, Morocco, 2008
Ph.D.: Physical Sciences, Ibn Zohr University, Rabat, Morocco, 2021
Scientific Position: Prof., Mohammadia School of Engineers, Mohammed V University, Rabat, Morocco, 2022
Research Interests: Computational fluid mechanics
Scientific Publications: 10 Papers, 3 Projects, 1 Thesis

Name: **Satyam**
Surname: **Panchal**
Birthday: 31.01.1975
Birthplace: Vallabh Vidyanagar, India
Bachelor: Mechanical Engineering, Sardar Patel University, India, 1998
Master-1: Mechanical Engineering, Maharaja Sayajirao University, Baroda, India, 2001
Master-2: Mechanical Engineering, University of Waterloo, Ontario, Canada, 2014
Ph.D.: Mechanical Engineering, Ontario Tech University, Oshawa, Ontario, Canada, 2017
Scientific Position: Adjunct Assist. Prof, Department of Mechanical and Mechatronics Engineering, University of Waterloo, Ontario, Canada, Since 2017
Research Interests: Lithium-Ion Battery, Safety and Performance, Thermal Management
Scientific Publications: 135 Papers, 3 Patents